Available online at www.sciencedirect.com
ScienceDirect
Journal of Computational Physics 226 (2007) 1444–1457
JOURNAL OF COMPUTATIONAL PHYSICS
www.elsevier.com/locate/jcp

The finite-volume time-domain algorithm using least square method in solving Maxwell's equations

Yan Shi *, Chang-Hong Liang

School of Electronic Engineering, Xidian University, Xi'an 710071, PR China

Received 26 December 2006; received in revised form 27 May 2007; accepted 30 May 2007
Available online 14 June 2007

Abstract

A finite-volume time-domain algorithm using least square method with a well-posed perfectly matched layer (PML) has been developed for the time-domain solution of Maxwell's equations. This algorithm uses the unstructured grids to obtain good computational efficiency and geometric flexibility. A novelty cell-wise data reconstruction scheme based on least square method is derived to achieve second-order spatial accuracy. A well-posed PML is applied to truncate computational domain by absorbing outgoing electromagnetic waves. The explicit Runge–Kutta scheme is employed to solve the semi-discrete Maxwell's equations. Several numerical results are presented to illustrate the efficiency and accuracy of the algorithm.

Keywords: Finite-volume time-domain (FVTD); Least square (LS); Well-posed; Perfectly matched layer (PML)

1. Introduction

Since the Maxwell's equations were established in 1873 [1,2], there have been considerably interests in the development of efficient techniques for solving Maxwell's equations. Analytical methods can provide fast solution and allow users to foresee the effects and trend of the solution according to individual parameters in the formulas. However, there are many geometric and physical limitations restricting the analytic models from general applications. The classical integral based solution technique [3], as unchallenged as they are for pure scattering problems, are less appealing for broadband applications and problems including penetration, complex materials and random effects. Finite element technique [4] can, at significant cost, successfully address some of these concerns but does so assuming monochromatic waves. This suggests that one turns the attention to time-domain methods for solving Maxwell's equations.

The most popular algorithm used in solving Maxwell's equations in time domain is undoubtedly finite difference time-domain (FDTD) method [5–7]. The simplicity, robustness and reasonable accuracy of FDTD

* Corresponding author. Tel.: +86 29 88204068; fax: +86 29 88201164.
E-mail address: shiyan@mail.xidian.edu.cn (Y. Shi).

0021-9991/$ - see front matter © 2007 Elsevier Inc. All rights reserved.
doi:10.1016/j.jcp.2007.05.033

method has propelled this method to be widely used and extended. In spite of its popularity, however, the main disadvantage with FDTD is its reduced accuracy when modeling curved and discontinuous objects.

In 1989, Shankar et al., developed a body-fitted non-orthogonal grid method called finite-volume time-domain (FVTD) method [8]. In recent years, FVTD method has been used successfully in computational fluid dynamics (CFD) [9–12] and computational electromagnetics (CEM) [13–20]. This method is used to solve the integral form of the conservation law with cell averages of the conservative variables as the unknowns. A reconstruction for each cell is obtained in terms of unknowns at neighboring cell. The flux integral for each face is evaluated by the reconstructed solution in two cells and an approximate Riemann solver. More recently, FVTD method was further refined and extended to unstructured grid [21–24]. With the unstructured grid technology, grid generation for complex geometries can be completely automated. However, due to the unstructured nature of grid, how to obtain a nonsingular stencil in data reconstruction becomes a key problem.

In this paper, we propose a FVTD algorithm using least square (LS) method with a well-posed perfectly matched layer (PML). The novelty LS method is derived for cell-wise data reconstruction to achieve second-order spatial accuracy. To model unbounded problems where electromagnetic waves propagate in an open region, the well-posed PML is applied to efficiently truncate the computational domain by absorbing outgoing electromagnetic waves. Accuracy, dispersion and stability of this algorithm are analyzed in detail. Several numerical results demonstrate good efficiency and accuracy.

2. Numerical scheme

2.1. Finite-volume discretization

We restrict our descriptions to two-dimensional cases although extension to 3D is straightforward. Consider an isotropic, conductive, inhomogeneous medium with electric permittivity ε, magnetic permeability μ and conductivity σ. For the 2D TM_z (transverse magnetic to z) polarization, Maxwell's equations take the form

$$Q\frac{\partial q}{\partial t}+\nabla\cdot F(q)+Dq=0 \tag{1}$$

in which

$$Q=\begin{bmatrix}\varepsilon & 0 & 0\\ 0 & \mu & 0\\ 0 & 0 & \mu\end{bmatrix},\quad q=\begin{bmatrix}E_z\\ H_x\\ H_y\end{bmatrix},\quad F=\begin{bmatrix}-H_y & H_x\\ 0 & E_z\\ -E_z & 0\end{bmatrix},\quad D=\begin{bmatrix}\sigma & 0 & 0\\ 0 & 0 & 0\\ 0 & 0 & 0\end{bmatrix}. \tag{2}$$

In finite-volume scheme, we first need to discretize the whole computational domain into small control volumes according to the problem geometry and material distribution. For geometric flexibility, consider each control volume as straightsided triangle cell. Then integrating (1) in an arbitrary control volume, we can obtain:

$$Q\frac{\partial q}{\partial t}\,\mathrm{d}S+\sum_{i=1}^{3}\hat{n}_i\cdot F_i\mathrm{d}l_i+Dq\mathrm{d}S=0 \tag{3}$$

where $\mathrm{d}S$ is the area of the control volume, $\hat{n}_i$ is the unit outward normal of edge i and $\mathrm{d}l_i$ is the length of edge i. Each control volume has a cell-averaged vector q, which is assumed to be located at the cell barycenter. Let us consider choices of the numerical flux F_i. As this flux is responsible for connecting the solution between two adjacent control volumes, its choices are clearly important.

One nature condition is that the resulting scheme must be consistent. In other words, the exact solution must satisfy the scheme when refining the grid. For general problem, an upwind flux is a good choice, namely,

$$\hat{n}\cdot F=\begin{bmatrix}-\hat{n}\times\frac{(Z\vec{H}+\hat{n}\times\vec{E})^{(1)}+(Z\vec{H}-\hat{n}\times\vec{E})^{(2)}}{Z^{(1)}+Z^{(2)}}\\ \hat{n}\times\frac{(Y\vec{E}-\hat{n}\times\vec{H})^{(1)}+(Y\vec{E}+\hat{n}\times\vec{H})^{(2)}}{Y^{(1)}+Y^{(2)}}\end{bmatrix} \tag{4}$$

where the superscript (1) and (2) denote two adjacent control volumes with normal direction $\hat{n}$ pointing from control volume (1) to control volume (2), and $\vec{E}^{(1)}$, $\vec{H}^{(1)}$, $\vec{E}^{(2)}$, $\vec{H}^{(2)}$ are electromagnetic fields at both sides of the common edge.

2.2. Data reconstruction using least square method

In order to evaluate the flux through an edge between two adjacent control volumes, we need to know electromagnetic fields at both sides of the common edge. This can be done through data reconstruction. A least square method is used in data reconstruction. In the following, we give data reconstruction schemes according to the different material distribution.

(1) Consider the same medium parameters between the control volume 0 and three control volumes around, i.e. control volume 1, 2 and 3, as shown in Fig. 1.
In this case, we employ the Taylor expansion to implement data reconstruction. Given arbitrary field variable $\phi(x,y)$, we can obtain:

$$\phi_j = \phi_0 + \phi_x(x_j - x_0) + \phi_y(y_j - y_0) \quad (j = 1,2,3) \tag{5}$$

in which $\phi_0 = \phi(x_0,y_0)$, $\phi_j = \phi(x_j,y_j)$, $\phi_x = \partial\phi/\partial x$ and $\phi_y = \partial\phi/\partial y$. $(x_l,y_l)(l = 0,1,2,3)$ is the barycenter coordinates of lth cell. Therefore, the gradients of $\phi(x,y)$ are constructed by the following least square reconstruction

$$\begin{bmatrix} \phi_x \\ \phi_y \end{bmatrix} = A \begin{bmatrix} \phi_1 - \phi_0 \\ \phi_2 - \phi_0 \\ \phi_3 - \phi_0 \end{bmatrix} \tag{6}$$

where

$$A = \frac{1}{L} \begin{bmatrix} I_{yy} & -I_{xy} \\ -I_{xy} & I_{xx} \end{bmatrix} \begin{bmatrix} x_1 - x_0 & x_2 - x_0 & x_3 - x_0 \\ y_1 - y_0 & y_2 - y_0 & y_3 - y_0 \end{bmatrix} \tag{7}$$

$$I_{xx} = \sum_{j=1}^{3} (x_j - x_0)^2 \quad I_{yy} = \sum_{j=1}^{3} (y_j - y_0)^2 \quad I_{xy} = \sum_{j=1}^{3} (x_j - x_0)(y_j - y_0) \tag{8}$$

$$L = I_{xx} I_{yy} - I_{xy}^2 \tag{9}$$

(2) Consider the control volume 0 adjacent to PEC. Here we implement data reconstruction according to two different cases, as shown in Fig. 2. For clear description, the edge j of the control volume 0 denotes

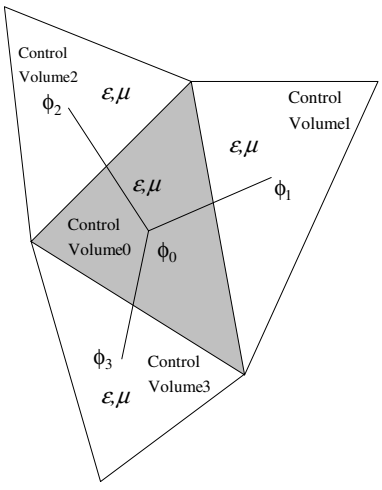

Fig. 1. Same medium between the control volume 0, 1, 2 and 3.

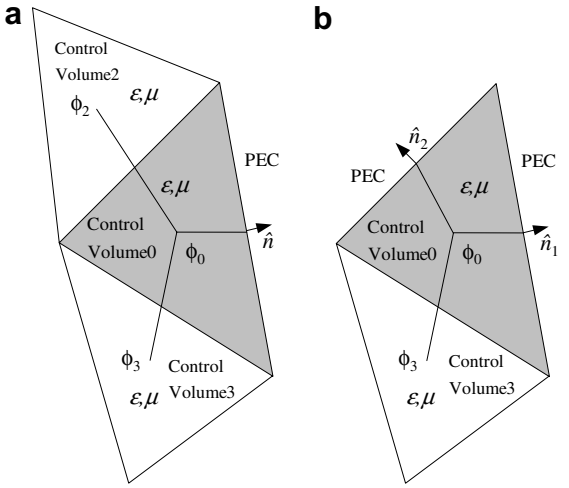

Fig. 2. The control volume 0 adjacent to PEC: (a) an edge adjacent to PEC and (b) two edges adjacent to PEC.

the common edge between the control volume 0 and j.

For the first case, without generality, suppose the control volume 1 located in PEC, as shown in Fig. 2a. At the midpoint of edge 1 of control volume 0, we implement the boundary conditions, i.e.,

$$E_z = 0 \tag{10}$$

$$n_x H_x + n_y H_y = 0 \tag{11}$$

For electric field reconstruction, we only need to substitute $\phi_1 = 0$ and the midpoint coordinates of the edge 1, i.e. (x_1^b, y_1^b), into (6). For the magnetic field reconstruction, we have

$$A \cdot \begin{bmatrix} \frac{\partial H_x^{(0)}}{\partial x} \\ \frac{\partial H_x^{(0)}}{\partial y} \\ \frac{\partial H_y^{(0)}}{\partial x} \\ \frac{\partial H_y^{(0)}}{\partial y} \end{bmatrix} = \begin{bmatrix} -n_x H_x^{(0)} - n_y H_y^{(0)} \\ H_x^{(2)} - H_x^{(0)} \\ H_x^{(3)} - H_x^{(0)} \\ H_y^{(2)} - H_y^{(0)} \\ H_y^{(3)} - H_y^{(0)} \end{bmatrix} \tag{12}$$

where $H_s^{(j)}(s = x, y)$ represents the magnetic field at the barycenter of control volume j, and

$$A = \begin{bmatrix} n_x(x_1^b - x_0) & n_x(y_1^b - y_0) & n_y(x_1^b - x_0) & n_y(y_1^b - y_0) \\ (x_2 - x_0) & (y_2 - y_0) & 0 & 0 \\ (x_3 - x_0) & (y_3 - y_0) & 0 & 0 \\ 0 & 0 & (x_2 - x_0) & (y_2 - y_0) \\ 0 & 0 & (x_3 - x_0) & (y_3 - y_0) \end{bmatrix} \tag{13}$$

We use LS method to solve $\left[\frac{\partial H_x^{(0)}}{\partial x} \quad \frac{\partial H_x^{(0)}}{\partial y} \quad \frac{\partial H_y^{(0)}}{\partial x} \quad \frac{\partial H_y^{(0)}}{\partial y}\right]^{\mathrm{T}}$, i.e.,

$$\begin{bmatrix} \frac{\partial H_x^{(0)}}{\partial x} \\ \frac{\partial H_x^{(0)}}{\partial y} \\ \frac{\partial H_y^{(0)}}{\partial x} \\ \frac{\partial H_y^{(0)}}{\partial y} \end{bmatrix} = (A^{\mathrm{T}}A)^{-1}A^{\mathrm{T}} \begin{bmatrix} -n_x H_x^{(0)} - n_y H_y^{(0)} \\ H_x^{(2)} - H_x^{(0)} \\ H_x^{(3)} - H_x^{(0)} \\ H_y^{(2)} - H_y^{(0)} \\ H_y^{(3)} - H_y^{(0)} \end{bmatrix} \tag{14}$$

For the second case, suppose the control volume 1 and 2 located in PEC, as shown in Fig. 2b. Similar to the first case, we can obtain:

$$\begin{bmatrix} \frac{\partial H_x^{(0)}}{\partial x} \\ \frac{\partial H_x^{(0)}}{\partial y} \\ \frac{\partial H_y^{(0)}}{\partial x} \\ \frac{\partial H_y^{(0)}}{\partial y} \end{bmatrix} = A^{-1} \begin{bmatrix} -n_{1x}H_x^{(0)} - n_{1y}H_y^{(0)} \\ -n_{2x}H_x^{(0)} - n_{2y}H_y^{(0)} \\ H_x^{(3)} - H_x^{(0)} \\ H_y^{(3)} - H_y^{(0)} \end{bmatrix} \tag{15}$$

in which

$$A = \begin{bmatrix} n_{1x}(x_1^b - x_0) & n_{1x}(y_1^b - y_0) & n_{1y}(x_1^b - x_0) & n_{1y}(y_1^b - y_0) \\ n_{2x}(x_2^b - x_0) & n_{2x}(y_2^b - y_0) & n_{2y}(x_2^b - x_0) & n_{2y}(y_2^b - y_0) \\ (x_3 - x_0) & (y_3 - y_0) & 0 & 0 \\ 0 & 0 & (x_3 - x_0) & (y_3 - y_0) \end{bmatrix} \tag{16}$$

Here (x_1^b, y_1^b) and (x_2^b, y_2^b) are the midpoint coordinates of the edge 1 and 2, respectively, and n_{is} $(s = x, y)$ is s-component of unit outward normal of the edge i.

(3) Consider the different medium in the control volume 0, 1, 2 and 3. Here we still divide into two different cases, as shown in Fig. 3.

For the first case, suppose different medium in the control volume 0 and 1, as shown in Fig. 3a. At the midpoint of the edge 1 of control volume 0, we implement the boundary conditions, i.e.,

$$E_z^{(0)} = E_z^{(1)} \tag{17}$$

$$-n_y H_x^{(0)} + n_x H_y^{(0)} = -n_y H_x^{(1)} + n_x H_y^{(1)} \tag{18}$$

$$\mu(n_x H_x^{(0)} + n_y H_y^{(0)}) = \mu_1(n_x H_x^{(1)} + n_y H_y^{(1)}) \tag{19}$$

where the superscript (i) denotes the control volume i.

Considering the continuous tangential component of electric field, i.e. (17), we can still use (6) for the electric field reconstruction. For the magnetic field reconstruction, we will have

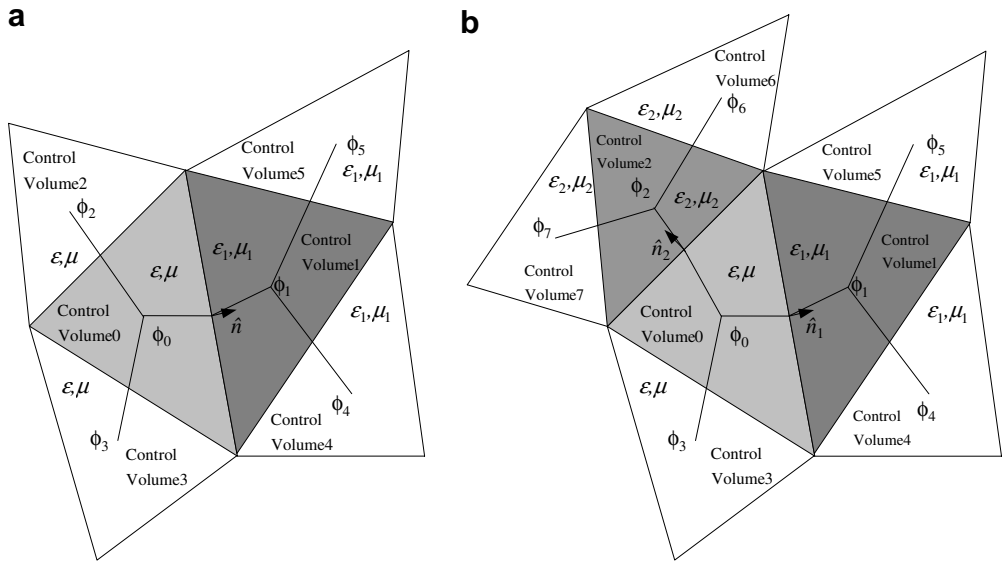

Fig. 3. Different medium in the control volume 0, 1, 2 and 3: (a) different medium in control volume 0 and 1 and (b) different medium in control volume 0, 1 and 2.

$$A \cdot \begin{bmatrix} \frac{\partial H_x^{(0)}}{\partial x} \\ \frac{\partial H_x^{(0)}}{\partial y} \\ \frac{\partial H_y^{(0)}}{\partial x} \\ \frac{\partial H_y^{(0)}}{\partial y} \\ \frac{\partial H_x^{(1)}}{\partial x} \\ \frac{\partial H_x^{(1)}}{\partial y} \\ \frac{\partial H_y^{(1)}}{\partial x} \\ \frac{\partial H_y^{(1)}}{\partial y} \end{bmatrix} = \begin{bmatrix} n_y(H_x^{(1)} - H_x^{(0)}) - n_x(H_y^{(1)} - H_y^{(0)}) \\ n_x(\mu_1 H_x^{(1)} - \mu H_x^{(0)}) + n_y(\mu_1 H_y^{(1)} - \mu H_y^{(0)}) \\ H_x^{(2)} - H_x^{(0)} \\ H_x^{(3)} - H_x^{(0)} \\ H_y^{(2)} - H_y^{(0)} \\ H_y^{(3)} - H_y^{(0)} \\ H_x^{(4)} - H_x^{(1)} \\ H_x^{(5)} - H_x^{(1)} \\ H_y^{(4)} - H_y^{(1)} \\ H_y^{(5)} - H_y^{(1)} \end{bmatrix} \tag{20}$$

where

$$A = \begin{bmatrix} n_y x_b^{10} & n_y y_b^{10} & -n_x x_b^{10} & -n_x y_b^{10} & -n_y x_b^{11} & -n_y y_b^{11} & n_x x_b^{11} & n_x y_b^{11} \\ n_x \mu x_b^{10} & n_x \mu y_b^{10} & n_y \mu x_b^{10} & n_y \mu y_b^{10} & -n_x \mu_1 x_b^{11} & -n_x \mu_1 y_b^{11} & -n_y \mu_1 x_b^{11} & -n_y \mu_1 y_b^{11} \\ x^{20} & y^{20} & 0 & 0 & 0 & 0 & 0 & 0 \\ x^{30} & y^{30} & 0 & 0 & 0 & 0 & 0 & 0 \\ 0 & 0 & x^{20} & y^{20} & 0 & 0 & 0 & 0 \\ 0 & 0 & x^{30} & y^{30} & 0 & 0 & 0 & 0 \\ 0 & 0 & 0 & 0 & x^{41} & y^{41} & 0 & 0 \\ 0 & 0 & 0 & 0 & x^{51} & y^{51} & 0 & 0 \\ 0 & 0 & 0 & 0 & 0 & 0 & x^{41} & y^{41} \\ 0 & 0 & 0 & 0 & 0 & 0 & x^{51} & y^{51} \end{bmatrix} \tag{21}$$

where $S^{ij} = S_i - S_j$ and $S_b^{ij} = S_i^b - S_j (S = x, y; i, j = 1, 2, 3, 4, 5)$. The gradients of H_x and H_y in the control volume 0 and 1 can be together obtained using LS method.

For the second case, we can similarly obtain:

$$A \cdot U = B \tag{22}$$

in which

$$U = \left[\frac{\partial H_x^{(0)}}{\partial x} \quad \frac{\partial H_x^{(0)}}{\partial y} \quad \frac{\partial H_y^{(0)}}{\partial x} \quad \frac{\partial H_y^{(0)}}{\partial y} \quad \frac{\partial H_x^{(1)}}{\partial x} \quad \frac{\partial H_x^{(1)}}{\partial y} \quad \frac{\partial H_y^{(1)}}{\partial x} \quad \frac{\partial H_y^{(1)}}{\partial y} \quad \frac{\partial H_x^{(2)}}{\partial x} \quad \frac{\partial H_x^{(2)}}{\partial y} \quad \frac{\partial H_y^{(2)}}{\partial x} \quad \frac{\partial H_y^{(2)}}{\partial y} \right]^{\mathrm{T}} \tag{23}$$

$$B = \begin{bmatrix} n_{1y}(H_x^{(1)} - H_x^{(0)}) - n_{1x}(H_y^{(1)} - H_y^{(0)}) \\ n_{1x}(\mu_1 H_x^{(1)} - \mu H_x^{(0)}) + n_{1y}(\mu_1 H_y^{(1)} - \mu H_y^{(0)}) \\ n_{2y}(H_x^{(2)} - H_x^{(0)}) - n_{2x}(H_y^{(2)} - H_y^{(0)}) \\ n_{2x}(\mu_2 H_x^{(2)} - \mu H_x^{(0)}) + n_{2y}(\mu_2 H_y^{(2)} - \mu H_y^{(0)}) \\ H_x^{(3)} - H_x^{(0)} \\ H_y^{(3)} - H_y^{(0)} \\ H_x^{(4)} - H_x^{(1)} \\ H_x^{(5)} - H_x^{(1)} \\ H_y^{(4)} - H_y^{(1)} \\ H_y^{(5)} - H_y^{(1)} \\ H_x^{(6)} - H_x^{(2)} \\ H_x^{(7)} - H_x^{(2)} \\ H_y^{(6)} - H_y^{(2)} \\ H_y^{(7)} - H_y^{(2)} \end{bmatrix} \tag{24}$$

$$A = \begin{bmatrix}
n_{1y}x_b^{10} & n_{1y}y_b^{10} & -n_{1x}x_b^{10} & -n_{1x}y_b^{10} & -n_{1y}x_b^{11} & -n_{1y}y_b^{11} & n_{1x}x_b^{11} & n_{1x}y_b^{11} & 0 & 0 & 0 & 0 \\
n_{1x}\mu x_b^{10} & n_{1x}\mu y_b^{10} & n_{1y}\mu x_b^{10} & n_{1y}\mu y_b^{10} & -n_{1x}\mu_1 x_b^{11} & -n_{1x}\mu_1 y_b^{11} & -n_{1y}\mu_1 x_b^{11} & -n_{1y}\mu_1 y_b^{11} & 0 & 0 & 0 & 0 \\
n_{2y}x_b^{20} & n_{2y}y_b^{20} & -n_{2x}x_b^{20} & -n_{2x}y_b^{20} & 0 & 0 & 0 & 0 & -n_{2y}x_b^{22} & -n_{2y}y_b^{22} & n_{2x}x_b^{22} & n_{2x}y_b^{22} \\
n_{2x}\mu x_b^{20} & n_{2x}\mu y_b^{20} & n_{2y}\mu x_b^{20} & n_{2y}\mu y_b^{20} & 0 & 0 & 0 & 0 & -n_{2x}\mu_2 x_b^{22} & -n_{2x}\mu_2 y_b^{22} & -n_{2y}\mu_2 x_b^{22} & -n_{2y}\mu_2 y_b^{22} \\
x^{30} & y^{30} & 0 & 0 & 0 & 0 & 0 & 0 & 0 & 0 & 0 & 0 \\
0 & 0 & x^{30} & y^{30} & 0 & 0 & 0 & 0 & 0 & 0 & 0 & 0 \\
0 & 0 & 0 & 0 & x^{41} & y^{41} & 0 & 0 & 0 & 0 & 0 & 0 \\
0 & 0 & 0 & 0 & x^{51} & y^{51} & 0 & 0 & 0 & 0 & 0 & 0 \\
0 & 0 & 0 & 0 & 0 & 0 & x^{41} & y^{41} & 0 & 0 & 0 & 0 \\
0 & 0 & 0 & 0 & 0 & 0 & x^{51} & y^{51} & 0 & 0 & 0 & 0 \\
0 & 0 & 0 & 0 & 0 & 0 & 0 & 0 & x^{62} & y^{62} & 0 & 0 \\
0 & 0 & 0 & 0 & 0 & 0 & 0 & 0 & x^{72} & y^{72} & 0 & 0 \\
0 & 0 & 0 & 0 & 0 & 0 & 0 & 0 & 0 & 0 & x^{62} & y^{62} \\
0 & 0 & 0 & 0 & 0 & 0 & 0 & 0 & 0 & 0 & x^{72} & y^{72}
\end{bmatrix} \tag{25}$$

Similarly, the gradients of H_x and H_y in the control volume 0, 1 and 2 can be obtained using LS method. From derivation above, we can know that due to the consideration of the boundary conditions, the dimensions of gradient equations of H_x and H_y are correspondingly increased. However, as the matrix A only depends on the geometries and materials, the least-square inversion may be done in preprocessing stage. This greatly increases computational efficiency. For a practical problem, on the other hand, boundary conditions are not considered in most of the control volumes. Therefore, introduction of boundary conditions into the gradient equations of H_x and H_y not only promises good accuracy but also keeps original computational speed. In order to clearly show the efficiency of our method, we make a comparison between our method and discontinuous galerkin method (DGM) [25]. The efficiency of our method can be approximately given as $N_d^2 \cdot N_t$, in which N_t is the number of all control volumes and N_d is the dimension of matrix A. For most of control volumes belong to the first case, N_d is approximately equal to 3. The efficiency of DGM can be given as $N_n^2 \cdot N_t$, in which N_t is the number of all control volumes and N_n is the number of nodal points in each volume. In two-dimensional case, N_n is set as 6 to obtain solution with two-order spatial approximation accuracy. By comparison, the efficiency of our method is better than that of DGM.

2.3. Well-posed PML

A key issue in time-domain solution is the introduction of an absorbing boundary condition to truncate the unbounded medium to enable the solution in a finite computational domain without introducing noticeable reflections from the computational edge [26–28]. Here we adopt the unsplit-field well-posed PML formulations [28].

$$\frac{\partial \widetilde{H}_x}{\partial t} = -\frac{1}{\mu}\frac{\partial E_z}{\partial y} + (w_x - w_y)(\widetilde{H}_x - w_x Q_x) \tag{26}$$

$$\frac{\partial \widetilde{H}_y}{\partial t} = \frac{1}{\mu}\frac{\partial E_z}{\partial x} + (w_y - w_x)(\widetilde{H}_y - w_y Q_y) \tag{27}$$

$$\frac{\partial E_z}{\partial t} = \frac{1}{\varepsilon}\left[\frac{\partial \widetilde{H}_y}{\partial x} - \frac{\partial \widetilde{H}_x}{\partial y}\right] - \left(w_x + w_y + \frac{\sigma}{\varepsilon}\right)E_z - \left[w_x w_y + \frac{\sigma}{\varepsilon}(w_x + w_y)\right]P_z - \frac{\sigma}{\varepsilon}w_x w_y K_z \tag{28}$$

where

$$\frac{\partial Q_x}{\partial t} = \widetilde{H}_x - w_x Q_x \quad \frac{\partial Q_y}{\partial t} = \widetilde{H}_y - w_y Q_y \tag{29}$$

$$\frac{\partial P_z}{\partial t} = E_z \quad \frac{\partial K_z}{\partial t} = P_z \tag{30}$$

Note that this nonsplit PML is well-posed because (26)–(30) remain the same symmetric hyperbolic system as the original Maxwell's equations plus some lower-order terms [26,27]. When $w_x = w_y = 0$, the PML equations reduce to Maxwell' equations in a regular medium.

2.4. Time integration

In this paper, we adopt 2*N*-storage, *M*-stage *K*th -order Runge–Kutta scheme [29] to integrate (1) in each control volume. Expressing (1) as

$$\frac{\partial q}{\partial t} = f(t, q) \tag{31}$$

We denote q_n as $q(t_n)$ where $t_n = n\Delta t$ and Δt is the time step size. The low-storage form of Runge–Kutta method is given as

$$\begin{aligned} &u_0 = q_n \\ &\forall j \in [1, M] \\ &\begin{cases} k_j = a_j k_{j-1} + \Delta t f((n + c_j)\Delta t, u_{j-1}) \\ u_j = u_{j-1} + b_j k_j \end{cases} \\ &q_{n+1} = u_M \end{aligned} \tag{32}$$

where choices of coefficients a_j, b_j and c_j can be found in [29].

2.5. Analysis of accuracy, dispersion and stability

Firstly, let us consider the accuracy of FVTD algorithm above. Suppose one-dimensional Maxwell's equations in lossless and homogeneous medium

$$Q\frac{\partial q}{\partial t} + \nabla \cdot F(q) = 0 \tag{33}$$

in which

$$Q = \begin{bmatrix} \varepsilon & 0 \\ 0 & \mu \end{bmatrix}, \quad q = \begin{bmatrix} E^z \\ H^y \end{bmatrix}, \quad F = \begin{bmatrix} -H^y \\ -E^z \end{bmatrix}. \tag{34}$$

Assume that a uniform mesh $x_i = i\Delta x$ is used to solve (33), and q is the cell-averaged state-variable at the ith cell $[x_i, x_{i+1}]$. In the ith cell, the gradient of state-variable q can be obtained by using Least-Square method, i.e.

$$\frac{\partial q}{\partial x} = \frac{q_{i+1} - q_{i-1}}{2\Delta x} \tag{35}$$

This is equivalent to two-order MUSCL method [9]. Therefore, the space discretization is second-order accuracy. Temporal integration approximation of (33) is done using a low-storage Runge–Kutta scheme. When a two-stage second-order Runge–Kutta scheme is used, the overall numerical scheme is a second order accuracy in space and time. When a five-stage fourth-order Runge–Kutta scheme is adopted, the overall numerical scheme is a second order accuracy in space and fourth order accuracy in time.

In the following, we derive the numerical dispersion relation of FVTD in detail. Without generality, the two-order central difference approximation is used for time derivatives in (33). Substituting (35) into (33), we can obtain:

$$\varepsilon\frac{\partial E_i^z}{\partial t}\Delta x + \frac{H_{i+2}^y - 6H_{i+1}^y + 6H_{i-1}^y - H_{i-2}^y}{8} + \frac{E_{i+2}^z - 4E_{i+1}^z + 6E_i^z - 4E_{i-1}^z + E_{i-2}^z}{8\mu c} = 0 \tag{36}$$

$$\mu\frac{\partial H_i^y}{\partial t}\Delta x + \frac{E_{i+2}^z - 6E_{i+1}^z + 6E_{i-1}^z - E_{i-2}^z}{8} + \frac{H_{i+2}^y - 4H_{i+1}^y + 6H_i^y - 4H_{i-1}^y + H_{i-2}^y}{8\varepsilon c} = 0 \tag{37}$$

Moreover, assume plane monochromatic traveling-wave trial solutions as follows:

$$E_i^{z,n} = E_0 \mathrm{e}^{\mathrm{j}\omega n\Delta t}\mathrm{e}^{-\mathrm{j}ki\Delta x} \tag{38}$$

$$H_i^{y,n} = H_0 \mathrm{e}^{\mathrm{j}\omega n\Delta t}\mathrm{e}^{-\mathrm{j}ki\Delta x} \tag{39}$$

Substituting (38) and (39) into (36) and (37), and approximating time derivatives by central difference yield

$$\begin{bmatrix} A_{11} & A_{12} \\ A_{21} & A_{22} \end{bmatrix} \begin{bmatrix} E_0 \\ H_0 \end{bmatrix} = \begin{bmatrix} 0 \\ 0 \end{bmatrix} \tag{40}$$

where

$$A_{11} = \frac{\varepsilon\Delta x}{\Delta t}\left(\mathrm{j}2\sin\frac{\omega\Delta t}{2}\right) + \frac{1}{4\mu c}\left(\cos\frac{\omega\Delta t}{2}\right)(\cos 2k\Delta x - 4\cos k\Delta x + 3) \tag{41}$$

$$A_{22} = \frac{\mu\Delta x}{\Delta t}\left(\mathrm{j}2\sin\frac{\omega\Delta t}{2}\right) + \frac{1}{4\varepsilon c}\left(\cos\frac{\omega\Delta t}{2}\right)(\cos 2k\Delta x - 4\cos k\Delta x + 3) \tag{42}$$

$$A_{12} = A_{21} = \frac{\mathrm{j}}{4}(6\sin k\Delta x - \sin 2k\Delta x) \tag{43}$$

In order to ensure (40) with non-zero solution, the numerical dispersion relation can be obtained as follows:

$$\left(\frac{\Delta x}{c\Delta t}\right)^2\left(2\sin\frac{\omega\Delta t}{2}\right)^2 = \left(\cos\frac{\omega\Delta t}{2}\right)^2\left(\frac{\cos 2k\Delta x - 4\cos k\Delta x + 3}{4}\right)^2 + \left(\frac{6\sin k\Delta x - \sin 2k\Delta x}{4}\right)^2 + \frac{\Delta x}{2c\Delta t}(j\sin\omega\Delta t)(\cos 2k\Delta x - 4\cos k\Delta x + 3) \tag{44}$$

The numerical wave vector k in (44) can be solved by using iterative Newton's procedure [6]. It can be seen from (44) that the numerical wave vector k is complex for real angular frequency ω. Therefore, there is an unphysical behavior called parasite in FVTD [30]. The phenomenon is mainly because electric fields and magnetic fields are un-staggered in FVTD scheme. However by a lot of numerical experiments, we can know that the parasite has no serious effect on numerical solution, when appropriate time step and spatial mesh are chosen. The mainly reason is that when $\Delta x \to 0$, (44) can be reduced to

$$\left(\frac{\Delta x}{c\Delta t}\right)\left(2\sin\frac{\omega\Delta t}{2}\right) = (k\Delta x) \tag{45}$$

Furthermore when $\Delta t \to 0$, we can obtain the exact dispersion relation from (45) as follows:

$$\frac{\omega}{c} = k \tag{46}$$

Finally, we give the stability analysis of FVTD algorithm in detail. The explicit forward Euler scheme is adopted to approximate time derivative in (33). Therefore we can obtain:

$$E_i^{z,n+1} = E_i^{z,n} - \frac{\Delta t}{\varepsilon\Delta x}\frac{H_{i+2}^{y,n} - 6H_{i+1}^{y,n} + 6H_{i-1}^{y,n} - H_{i-2}^{y,n}}{8} - \frac{c\Delta t}{\Delta x}\frac{E_{i+2}^{z,n} - 4E_{i+1}^{z,n} + 6E_i^{z,n} - 4E_{i-1}^{z,n} + E_{i-2}^{z,n}}{8} \tag{47}$$

$$H_i^{y,n+1} = H_i^{y,n} - \frac{\Delta t}{\mu\Delta x}\frac{E_{i+2}^{z,n} - 6E_{i+1}^{z,n} + 6E_{i-1}^{z,n} - E_{i-2}^{z,n}}{8} - \frac{c\Delta t}{\Delta x}\frac{H_{i+2}^{y,n} - 4H_{i+1}^{y,n} + 6H_i^{y,n} - 4H_{i-1}^{y,n} + H_{i-2}^{y,n}}{8} \tag{48}$$

Similarly, assume the following plane monochromatic traveling-wave trial solutions:

$$E^{z,n} = E_0^n \mathrm{e}^{-\mathrm{j}kx} \tag{49}$$

$$H^{y,n} = H_0^n \mathrm{e}^{-\mathrm{j}kx} \tag{50}$$

Substituting (49) and (50) into (47) and (48), after simplification, we can obtain:

$$\begin{bmatrix} E_i^{z,n+1} \\ H_i^{y,n+1} \end{bmatrix} = B \cdot \begin{bmatrix} E_i^{z,n} \\ H_i^{y,n} \end{bmatrix} = \begin{bmatrix} B_{11} & B_{12} \\ B_{21} & B_{22} \end{bmatrix} \begin{bmatrix} E_i^{z,n} \\ H_i^{y,n} \end{bmatrix} \tag{51}$$

in which

$$B_{11} = B_{22} = 1 - \frac{c\Delta t}{4\Delta x}(\cos 2k\Delta x - 4\cos k\Delta x + 3) \tag{52}$$

$$B_{12} = -\frac{j}{4}\frac{\Delta t}{\varepsilon \Delta x}(6\sin k\Delta x - \sin 2k\Delta x) \tag{53}$$

$$B_{21} = -\frac{j}{4}\frac{\Delta t}{\mu \Delta x}(6\sin k\Delta x - \sin 2k\Delta x) \tag{54}$$

The stability requires $\rho(B) \leqslant 1$, where $\rho(B)$ is spectral radius of matrix B. The eigenvalues of B can be determined analytically as

$$\lambda = B_{11} \pm \frac{B_{12}}{\eta} \tag{55}$$

The maximum of λ for all possible values of k is

$$|\lambda_{\max}| = \left|\frac{2c\Delta t}{\Delta x} - 1\right| \tag{56}$$

If $\rho(B) \leqslant 1$, then $|\lambda_{\max}| \leqslant 1$. Hence, this leads to stability limit as follows

$$c\Delta t \leqslant \Delta x \tag{57}$$

Therefore, the explicit forward Euler scheme is stable when the CFL number $c\Delta t/\Delta x$ is less than 1. The general stability condition of explicit Runge–Kutta scheme for two-dimensional and three-dimensional FVTD method on arbitrary unstructured mesh can be found in reference [31].

3. Numerical results and discussion

In this section, we present some numerical examples to demonstrate the accuracy and efficiency of the FVTD algorithm using LS method. All calculations were performed on a Pentium IV 3.0 GHz PC with 1GB memory.

3.1. Scattering by a perfectly electrical conductor (PEC) circular cylinder

Let us consider the plane wave scattering from a perfect conductor cylinder in free space. A plane wave is incident along $+x$-axis on the cylinder. The radius of perfect conductor cylinder is $2m$ and the center of the cylinder is set as origin. The exact frequency-domain solution of problem is [1]

$$E_z = \sum_{n=-\infty}^{\infty}\left[J_n(k\rho) - \frac{J_n(ka)}{H_n^{(1)}(ka)}H_n^{(1)}(k\rho)\right] \cdot \mathrm{e}^{\mathrm{i}n\varphi - \mathrm{i}n\pi/2} \tag{58}$$

in which $k = 2\pi f/c$ is wave number in free space. The time solution can be obtained by Fourier transform of frequency-domain solution. In this example we adopt 2930 triangles to mesh the whole computational domain in order to obtain a resolution of 15 points of per wavelength (ppw). In our calculation $\Delta t = 1$ ps and the observation point is located at $(-1.695, -1.816)$ m. Control volumes used in the calculation are shown in Fig. 4a. The FVTD algorithm using LS method is implemented to calculate the scattering electric field E_z at the observation point. Fig. 4b illustrates comparison between the result of this algorithm and the analytical solution, showing the excellent agreement.

In order to further test the accuracy of this algorithm, we employ the FVTD algorithm using LS method to recalculate the plane wave scattering from a perfect conductor cylinder. The variation of logarithm of relative error with the points of per wavelength is given in Fig. 5. From Fig. 5, it can be clearly seen that relative error

is decreased with increase of the points of per wavelength and the second-order accuracy can be obtained in our algorithm.

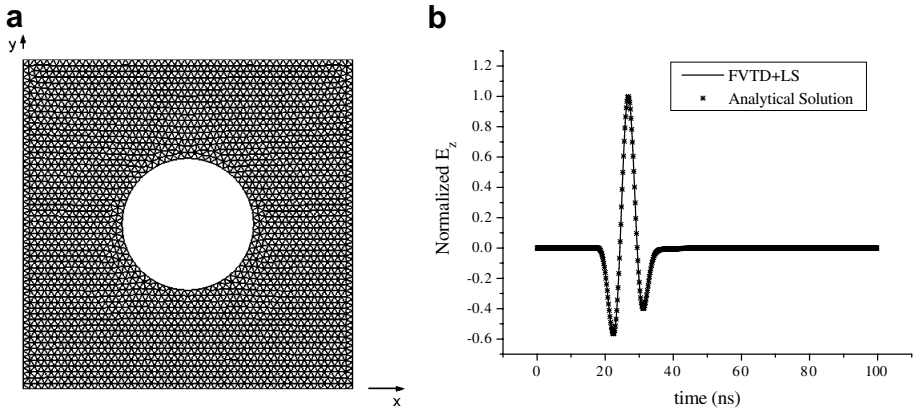

Fig. 4. Plane wave scattering from a PEC circular cylinder in free space: (a) grid and (b) comparison of solution of the FVTD + LS with the analytical solution.

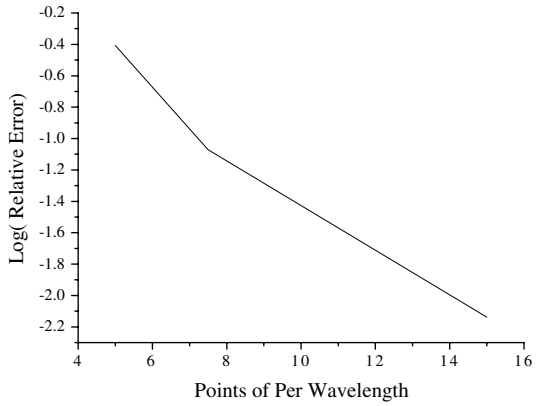

Fig. 5. Accuracy of FVTD algorithm using LS method.

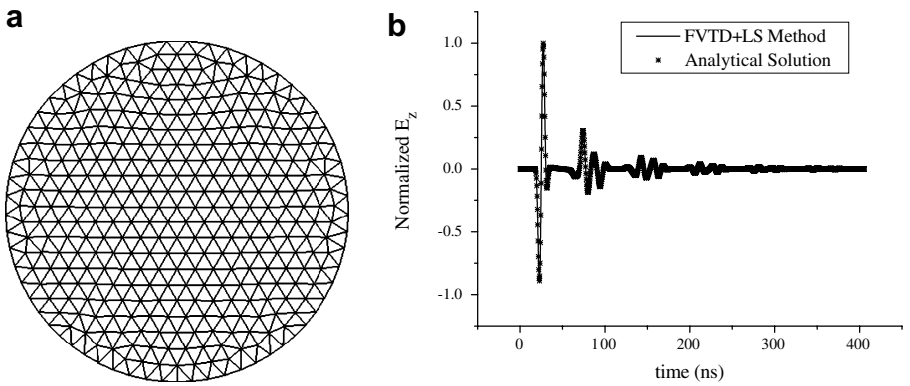

Fig. 6. Plane wave scattering from a dielectric circle cylinder in free space: (a) grid and (b) comparison of solution of the FVTD + LS with the analytical solution.

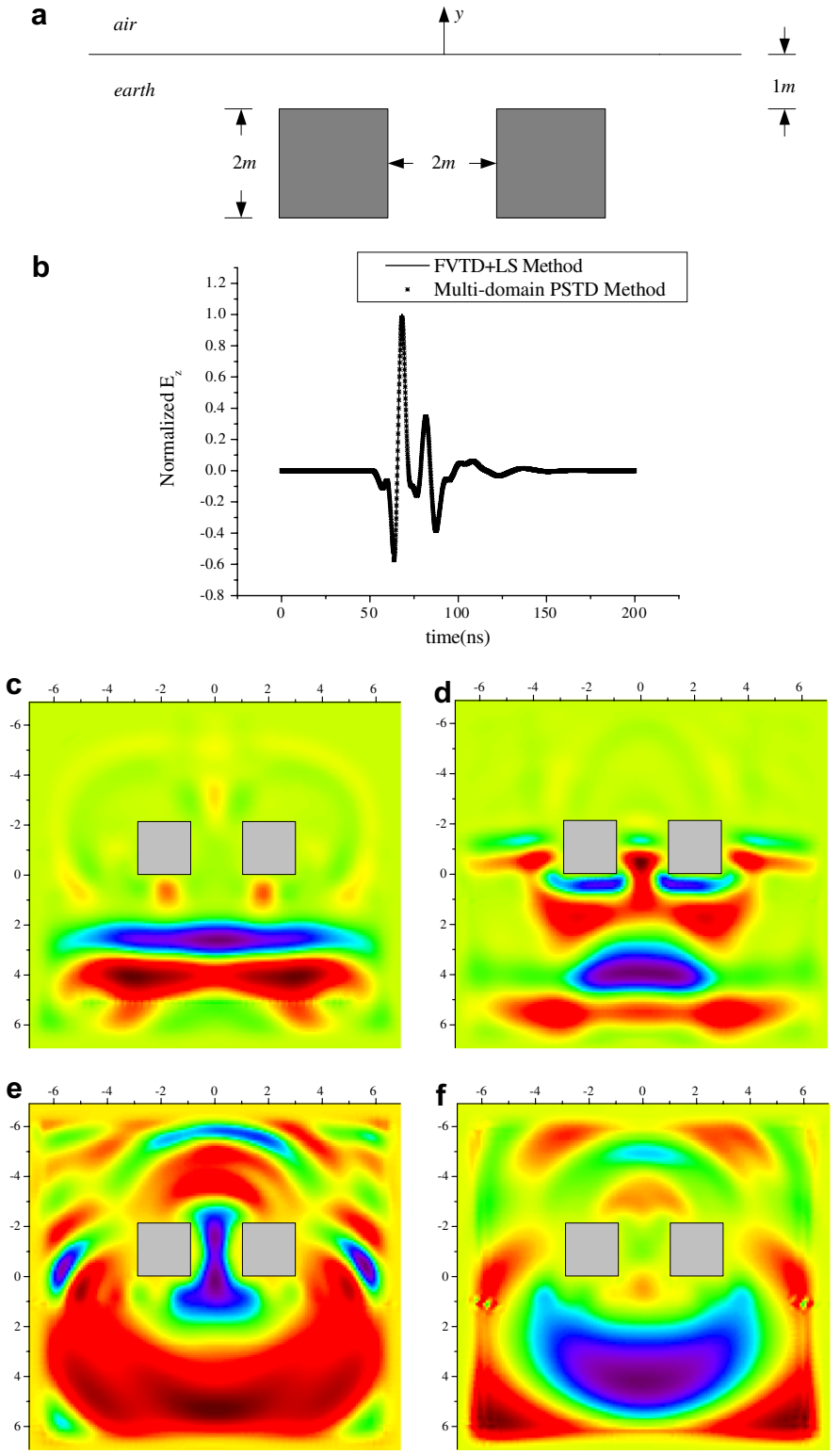

Fig. 7. Plane wave scattering from the buried PEC objects in a lossy half space: (a) geometry, (b) comparison of solution of FVTD + LS with solution of PSTD, (c) the snapshot taken at $t = 60$ ns, (d) the snapshot taken at $t = 80$ ns, (e) the snapshot taken at $t = 120$ ns and (f) the snapshot taken at $t = 160$ ns.

3.2. Scattering by a dielectric circular cylinder

The scattering by a dielectric circular cylinder with $\varepsilon_r = 4.0$ and $\mu_r = 1.0$ is computed by using FVTD + LS algorithm. A plane wave is incident along the $+x$-axis on the cylinder. The radius of dielectric circular cylinder is 2 m and the center of the cylinder is set as origin. The total number of control volumes is 3708 and the PPW is 15. The time step Δt is set as 0.5 ps and the receiver is located at $(-1.695, -1.816)$ m. Fig. 6a shows the control volumes in the dielectric circular cylinder. Fig. 6b demonstrates the comparison of the present algorithm and analytical solution. The two curves are nearly graphically indistinguishable.

3.3. Ground penetrating radar (GPR) detection of buried object

Ground penetrating radar (GPR) is a noninvasive electromagnetic geophysical technique for subsurface exploration, characterization and monitoring. It is used as a scientific tool in many areas such as geophysics respecting, archeology and environmental engineering. GPR has been put in a variety of uses, especially in detecting buried objects. Consider an application of FVTD + LS algorithm to GPR detection of buried objects. In this example, the electric parameters of the earth are $\varepsilon_r = 4$ and $\mu_r = 1$ and $\sigma = 0.002$ s/m. Two square PEC boxes are buried 1 m below the interface of air and earth, as shown in Fig. 7a. A plane wave is incident along the y-axis. The time-domain waveform of electric field at the receiver $(0.333, 1.417$ m) is calculated. The comparison between the present algorithm and multi-domain pseudospectral time-domain (PSTD) method [32] is shown in Fig. 7b. In Fig. 7c–f, we show the snapshots of the electric field at $t = 60$, 80, 120 and 160 ns over the whole simulation space.

4. Conclusions

A FVTD algorithm using LS method with a well-posed PML has been developed to model electromagnetic scattering by 2D arbitrarily curved objects in this paper. Considering computational efficiency and geometric flexibility, the unstructured grids are employed in this algorithm. The novelty LS method is used to derive cell-wise data reconstruction. The Runge–Kutta explicit scheme is employed to solve the semi-discrete Maxwell's equations. Accuracy, dispersion and stability of this algorithm are analyzed in detail. Several numerical examples confirm the capability and accuracy of the algorithm.

References

[1] R.F. Harrington, Time-Harmonic Electromagnetic Fields, McGrwa-Hill, New York, 1961.
[2] J.A. Kong, Electromagnetic Wave Theory, John Wiley, New York, 1986.
[3] R.F. Harrington, Field Computation by Moment Methods, MacMillan, New York, 1968.
[4] J.M. Jin, The Finite Element Method in Electromagnetics, John Wiley, New York, 1993.
[5] K.S. Yee, Numerical solution of initial boundary value problems involving Maxwell's equations in isotropic media, IEEE Trans. Antennas Propagat. 14 (1966) 302–307.
[6] A. Taflove, Computational Electrodynamics – The finite Difference Time-Domain Method, Artech House, Boston, 1995.
[7] K.S. Kunz, R.J. Luebbers, The Finite Difference Time Domain Method for Electroagnetics, CRC Press, Boca Raton, FL, 1993.
[8] V. Shankar, W.F. Hall, A.H. Mohammadian, A CFD-based finite-volume procedure for computational electromagnetics interdisciplinary applications of CFD methods AAIA-89-1987-CP, 1989.
[9] B.V. Leer, Towards the ultimate conservative difference scheme V. A second order sequel to Godunov's method, J. Comput. Phys. 32 (1979) 101–136.
[10] C. Hu, C.W. Shu, Weight essentially non-oscillatory schemes on triangular meshs, J. Comput. Phys. 150 (1999) 97–127.
[11] R. Abgrall, On essentially ono-oscillatory schemes on unstructured meshs: analysis and implementation, J. Comput. Phys. 114 (1994) 45–58.
[12] Z. Wang, Z.J. Wang, The lever set method on adaptive cartesian grid for interface capturing, AAIA-2004-0082, 2004.
[13] J.S. Shang, Characteristic-based algorithm for solving the Maxwell's equations in the time domain, IEEE Antennas Propagat. Mag. 37 (3) (1995) 15–25.
[14] K.S. Yee, J.S. Chen, The finite-difference time-domain (FDTD) and the finite-volume time-domain (FVTD) methods in solving Maxwell's equations, IEEE Trans. Antennas Propagat. 45 (3) (1997) 354–363.
[15] A.H. Mohammadian, V. Shankar, W.F. Hall, Computations of electromagnetic scattering and radiation using a time-domain finite-volume discretization procedure, Comput. Phys. Commun. 68 (1991) 175–196.

[16] J.S. Shang, R.M. Fithen, A comparative study of numerical algorithms for computational electromagnetics, AAIA-94-2410, 1994.
[17] D. Baumann, C. Fumeaux, P. Leuchtmann, R. Vahldieck, Finite volume time-domain (FVTD) method and its application to the analysis of hemispherical dielectric-resonator antennas, in: IEEE MTT-S Int. Microwave Symp. Dig., 2003, pp. 985–988.
[18] C. Fumeaux, D. Baumann, P. Leuchtmann, R. Vahldieck, A generalized local time-step for the FVTD method for efficient simulation of microwave antennas, in: 33rd Eur. Microwave Conf. Dig., 2003, pp. 467–470.
[19] C. Fumeaux, D. Baumann, P. Leuchtmann, R. Vahldieck, A generalized local time-step scheme for efficient FVTD simulations in strongly inhomogeneous meshes, IEEE Trans. Microwave Theory Tech. 52 (2003) 1067–1076.
[20] D. Baumann, C. Fumeaux, P. Leuchtmann, R. Vahldieck, Finite-volume time-domain (FVTD) modelling of a broadband double-ridged horn antenna, Int. J. Numer. Model: Electron. Networks Dev. Fields 17 (2004) 285–298.
[21] Y. Liu, A 3D high-order unstructured finite-volume algorithm for solving Maxwell's equations, in: 1995 Digest, USNC/NRSI Radio Science Meeting, 1995.
[22] Y. Liu, A generalized finite volume algorithm for solving the Maxwell's equations on arbitrary grids, in: Proceedings of 10th Annual Review of Progress in Applied Computational Electromagnetics, 1994.
[23] W.F. Hall, V. Shankar, S. Palaniswany, Algorithmic aspects of wave propagation through stretched unstructured cells for problems in computational electromagnetics, AAIA-97-2089, 1997.
[24] Z.J. Wang, A.J. Przekwas, Y. Liu, A FV-TD electromagnetic solver using adaptive cartesian grids, Comput. Phys. Commun. 148 (2002) 17–29.
[25] J.S. Hesthaven, T. Warburton, High-order nodal methods on unstructured grids. I. Time-domain solution of Maxwell's equations, J. Comput. Phys. 181 (2002) 186–221.
[26] S. Abarbanel, D. Gottlieb, On the construction and analysis of absorbing layers in CEM, in: Proceedings of the 13th Annual Review of Progress in Applied Computational Electromagnetics, 1997, pp. 876–883.
[27] S. Abarbanel, D. Gottlieb, A mathematical analysis of the PML method, J. Comput. Phys. 134 (1997) 357–363.
[28] G.X. Fan, Q.H. Liu, A strongly well-posed PML in lossy media, IEEE Antennas Wireless Propagat. Lett. 2 (2003) 97–100.
[29] M.H. Carpenter, C.A. Kennedy, Fourth order 2N-stroage Runge–Kutta scheme, NASA-TM-109112, 1994.
[30] D.R. Lynch, K.D. Paulsen, Origin of vector parasites in numerical maxwell solutions, IEEE Trans. Microwave Theory Tech. 39 (1991) 383–394.
[31] S. Piperno, L^2-stability of the upwind first order finite volume scheme for the Maxwell equations in two and three dimensions on arbitrary unstructured meshes, Math. Model. Numer. Anal. 34 (2000) 139–158.
[32] J.S. Hesthaven, P.G. Dinesen, J.P. Lynov, spectral collocation time-domain modeling of diffractive optical elements, J. Comput. Phys. 155 (1999) 287–306.